

A Topographic Drag Closure Built on an Analytical Base Flux

STEPHEN T. GARNER

NOAA/Geophysical Fluid Dynamics Laboratory, Princeton, New Jersey

(Manuscript received 23 March 2004, in final form 17 October 2004)

ABSTRACT

Topographic drag schemes depend on grid-scale representations of the average height, width, and orientation of the subgrid topography. Until now, these representations have been based on a combination of statistics and dimensional analysis. However, under certain physical assumptions, linear analysis provides the exact amplitude and orientation of the drag for arbitrary topography. The author proposes a computationally practical closure based on this analysis.

Also proposed is a nonlinear correction for nonpropagating base flux. This is patterned after existing schemes but is better constrained to match the linear solution because it assumes a correlation between mountain height and width. When the correction is interpreted as a formula for the transition to saturation in the wave train, it also provides a way of estimating the vertical distribution of the momentum forcing. The explicit subgrid height distribution causes a natural broadening of the layers experiencing the forcing. Linear drag due to simple oscillating flow over topography, which is relevant to ocean tides, has almost the same form as for the stationary atmospheric problem. However, dimensional analysis suggests that the nonpropagating drag in this situation is mostly due to topographic length scales that are small enough to keep the steady-state assumption satisfied.

1. Introduction

Mountain drag parameterizations estimate the total transfer of momentum across the topographic boundary (the base flux) as well as the convergence of the pseudomomentum flux as a function of height above the boundary. Previous schemes for estimating the base flux have relied entirely on statistical measures of the height, shape, and orientation of the unresolved terrain, guided by dimensional reasoning (e.g., Baines and Palmer 1990; Lott and Miller 1997; Scinocca and McFarlane 2000). Here I propose a scheme that uses an analytical estimate of the drag vector. This estimate is exact in the limit where the mountain waves are linear, inviscid, and hydrostatic, and the medium is nonrotating and uniform in time and space.

I also propose a correction for nonlinearity at the source. It is similar in many ways to existing schemes that allow a gradual transition between linear and nonlinear dimensional drag laws (e.g., Kim and Arakawa 1995, and references therein; Lott and Miller 1997; Sci-

nocca and McFarlane 2000). However, the proposed treatment exploits the correlation of mountain height with mountain width together with the known range of mountain heights within the grid cell. The motivation for adding this complexity is to produce a closer match to the analytical result in the linear limit as well as a less arbitrary transition to nonlinearity. A beneficial side effect is to make the overall scheme less tunable.

The impact of the subgrid topography on the resolved flow is due to the convergence of the pseudomomentum flux. A straightforward extension of the nonlinear base-flux correction yields an algorithm for clipping the flux to the saturation value as a function of height so as to determine this impact on the resolved flow. This part of the scheme adheres to traditional assumptions going back to Lindzen (1981), Palmer et al. (1986), and Pierrehumbert (1987).

2. Base-flux closure

Drag parameterizations for the atmosphere generally assume that the disturbance is steady and contains only upward-propagating waves. If we add to these assumptions certain constraints on the horizontal scale of the forcing, such that the waves are broad enough to be

Corresponding author address: Dr. Stephen T. Garner, NOAA/Geophysical Fluid Dynamics Laboratory, Princeton, NJ 08542.
E-mail: steve.garner@noaa.gov

hydrostatic but narrow enough to be unaffected by sphericity, rotation, horizontal shear, or baroclinicity, we can calculate the total drag in the linear limit as accurately as we know the shape of the terrain. This section begins with the linear analysis and then extends the scheme to deal with nonlinearity at the source.

a. Linear drag

We suppose that the topography can be analyzed into Fourier amplitudes $\hat{h}(\mathbf{k})$, where $\mathbf{k} = (k, l)$ is the horizontal wavenumber. This is permissible because the scales of interest are much smaller than the planetary scale. Let $\bar{V}_{\mathbf{k}} \equiv \bar{\mathbf{V}} \cdot \mathbf{k}/|\mathbf{k}|$ denote the component of the large-scale flow, $\bar{\mathbf{V}}$, parallel to \mathbf{k} . Then the linearized lower boundary condition is

$$\hat{W}(\mathbf{k}) = \bar{V}_{\mathbf{k}} i|\mathbf{k}| \hat{h}(\mathbf{k}), \quad (1)$$

where \hat{W} is the transform of $W(x, y) \equiv w(x, y, z = 0)$, the vertical velocity component at the ground. With this transform, it is assumed that all other spatial variability in the flow has much larger horizontal scales than the mountain waves.

It is also assumed that $d(|m|^{-1})/dz \ll 1$, where m is the stationary vertical wavenumber, and that $m \gg \bar{\rho}^{-1}|d\bar{\rho}/dz|$, where $\bar{\rho}(z)$ is the density profile. If we ignore horizontal variations of the buoyancy frequency, \bar{N} , and consider only hydrostatic scales $|\mathbf{k}| \ll m$, the Wentzel–Kramers–Brillouin (WKB) approximation for the vertical structure is

$$\hat{w}(\mathbf{k}, z) = \hat{W}(\mathbf{k}) \exp\left(i \int_0^z m dz'\right) \exp(z/2H), \quad (2)$$

with $H = \bar{\rho}/(-d\bar{\rho}/dz)$ and $m = \bar{N}/\bar{V}_{\mathbf{k}} + O(\lambda^2/H^2)$ (e.g., Holton 1973). Here λ denotes a scale for the vertical wavelength, inversely proportional to the typical m . It then follows from (1) and (2) that, at the surface,

$$\partial(\bar{\rho}\hat{w})/\partial z = -\bar{\rho}[\bar{N} + i\bar{V}_{\mathbf{k}}/(2H)]|\mathbf{k}|\hat{h} + O(\lambda^2/H^2). \quad (3)$$

Since there is no source of vertical vorticity at the ground, the horizontal velocity perturbation, say \mathbf{V}' , is completely determined by a scalar potential, $\chi(x, y)$, such that $\nabla\chi = \bar{\rho}\mathbf{V}'$. Here and in the following, ∇ denotes the horizontal operator. Conservation of mass implies $\nabla^2\chi = -\partial(\bar{\rho}w)/\partial z$, which, with (3), leads to

$$\hat{\chi}(\mathbf{k}) = -\bar{\rho}\bar{N} \frac{\hat{h}(\mathbf{k})}{|\mathbf{k}|} - \frac{\bar{\rho}}{2H} \frac{\hat{h}(\mathbf{k})}{|\mathbf{k}|^2} i\mathbf{k} \cdot \bar{\mathbf{V}}. \quad (4)$$

Here we have retained only the $O(\lambda/H)$ correction (the term involving $\bar{\mathbf{V}}$), which we call $\hat{\chi}_1$. The dominant first term, say $\hat{\chi}_0$, does not depend on the resolved wind and produces

$$\chi_0(x, y) = -\bar{\rho}\bar{N} \iint \frac{\hat{h}(\mathbf{k})}{|\mathbf{k}|} \exp(i\mathbf{k} \cdot \mathbf{x}) dk dl, \quad (5)$$

with $\mathbf{x} = (x, y)$. Thus, χ_0 is a slightly smoothed transformation of the terrain height. The velocity perturbation $(1/\bar{\rho})\nabla\chi_0$ produced by each spectral component of $h(x, y)$ is perpendicular to the corresponding phase lines of the topography and directed downhill.

If the integral in (5) converges, the spatial-transform equivalent is

$$\chi_0(x, y) = -\frac{\bar{\rho}\bar{N}}{2\pi} \iint \frac{h(\mathbf{x}')}{|\mathbf{x} - \mathbf{x}'|} dx' dy'. \quad (6)$$

The correction due to the vertical density gradient can also be put into the spatial domain. The easiest way is to define $A(x, y) = -\nabla^{-2}h$ so that $\chi_1 = -(\bar{\rho}/2H)\bar{\mathbf{V}} \cdot \nabla A$.

The integrals in (5) and (6) diverge if \hat{h} does not decrease as fast as $|\mathbf{k}|$ for small $|\mathbf{k}|$ (large scales). However, the result is already physically inconsistent at large scales. For both mathematical convergence and physical consistency, the input topography must be filtered to retain only the scales that force stationary, nonrotating gravity waves. Then, as a practical matter, (6) need not be integrated over the entire globe for each \mathbf{x} , but only over a radius equal to a small multiple of the high-pass filter scale. It is simplest to allow the topographic dataset to establish the low-pass scale. The problem of filtering is discussed by most drag-scheme developers, including Baines and Palmer (1990), Lott and Miller (1997), and Scinocca and McFarlane (2000). More is said about it below.

While the subgrid velocity perturbation is only weakly dependent on the resolved velocity (through the density gradient and χ_1), the momentum flux across a horizontal surface, namely,

$$\boldsymbol{\tau}(x, y) = \bar{\rho}w\mathbf{V}', \quad (7)$$

depends strongly on the resolved wind through $w = \bar{\mathbf{V}} \cdot \nabla h$. Let $\tilde{\chi} = (\rho_r N_r / \bar{\rho}\bar{N})\chi$, where the subscript r denotes constant reference values. Then

$$\boldsymbol{\tau} = \frac{\bar{\rho}\bar{N}}{\rho_r N_r} [\nabla\tilde{\chi}(\nabla h)^T]\bar{\mathbf{V}}. \quad (8)$$

The factor in brackets, $\nabla\tilde{\chi}(\nabla h)^T \equiv \mathbf{T}$, is the matrix product of two-dimensional vectors that depend only on the terrain, except for the small contribution from χ_1 . Subject to our assumptions, \mathbf{T} contains all relevant information about the topography, including amplitude, variance, orientation, and anisotropy. Using angle brackets to denote a grid-cell average, we can write

$$\langle \boldsymbol{\tau} \rangle = \frac{\bar{\rho} \bar{N}}{\rho_r N_r} \langle \mathbf{T} \rangle \bar{\mathbf{V}} \quad (9)$$

for the estimate of drag at a model grid point.

Because of the filtering, it should be consistent to regard (5) as an integral over spherical harmonics and to interpret $|\mathbf{k}|$ as the total spherical-harmonic wavenumber. Spherical-harmonic analysis of h is also a practical way to obtain the field $A(x, y)$ and the various second partial derivatives of A needed for \mathbf{T} . However, for the examples to follow, the flow disturbance was obtained from (6) and the small contribution from χ_1 was ignored. The topography was preprocessed using a spatial filter that passes only scales of less than about 1.5° of longitude and latitude in the extratropics. The filtering scale, d , was allowed to vary with latitude so as to keep the Rossby number, V/fd , of order unity, where $V(y)$ is a profile of typical surface wind speeds, and $f(y)$ is the Coriolis parameter. The horizontal derivatives in (8) make the result fairly insensitive to the choice of scales retained by a high-pass filter, and this allows a time-independent choice for $d(y)$.

Using a physical filter instead of a numerical one creates the danger of systematically overcounting the drag when the model grid spacing is smaller than d . With a physical filter, the subgrid drag has to be defined as the difference between the total parameterized drag and the model-dependent resolved drag, that is, the subgrid contribution is not known without diagnosing the resolved drag. In many climate-model applications, resolved drag can be neglected. This approach does not solve the problem of representing strong scale interactions near the grid scale—a generic problem of closures that also applies, for example, to moist convection schemes in both the time and space domain.

From (6), the velocity scales as $N_r h_r$, where h_r is a measure of the mesoscale component of the topographic height. Therefore, mountain wave velocities have an order of magnitude of $V \sim (10^{-2} \text{ s}^{-1})(10^3 \text{ m}) = 10 \text{ m s}^{-1}$, given a typical mesoscale relief of 1000 m. If the scale of the topography is 100 km and the ambient wind is of order 10 m s^{-1} , the vertical velocity is of order 0.1 m s^{-1} . It follows that the drag is characteristically $D \sim \rho_r (10 \text{ m s}^{-1}) (0.1 \text{ m s}^{-1}) \sim 1 \text{ Pa}$. The tensor \mathbf{T} is dominated by the diagonal elements, which are of the order of $\rho_r (10 \text{ m s}^{-1})$.

Shown in Fig. 1 is a plot of the linear drag $\langle \boldsymbol{\tau} \rangle$ over the Western Hemisphere for an assumed large-scale wind that is purely zonal at -7 m s^{-1} in the Tropics and 13 m s^{-1} in the extratropics. A constant buoyancy frequency, $N_r = 0.01 \text{ s}^{-1}$, and constant density, $\rho_r = 1 \text{ kg m}^{-3}$, are also assumed. The same calculation for the Asian continent, shown in Fig. 2, assumes a large-scale

wind from the west at 10 m s^{-1} everywhere. The averaging in both Fig. 1 and Fig. 2 is over latitude–longitude cells of about 1.5° on a side. The topographic dataset has a resolution of $1/30^\circ$.

b. Nonlinear extension

Nonlinearity is of the order of the nondimensional mountain height, $\tilde{h} = (\bar{N}/\bar{V})h$. We can write the lower boundary condition as a perturbation series based on \tilde{h} (e.g., Smith 1977):

$$w - \bar{\mathbf{V}} \cdot \nabla h = \mathbf{V}' \cdot \nabla h - \bar{\mathbf{V}} \cdot \nabla (\delta_z h) + h \bar{\mathbf{V}}_z \cdot \nabla h + \dots, \quad (10)$$

where δ is the lowest-order vertical particle displacement (with δ_z its first derivative) and $\bar{\mathbf{V}}_z$ is the resolved vertical shear. The first-order nonlinearities are represented by the three explicit terms on the right-hand side. The first two are associated with low-level blocking (e.g., Pierrehumbert and Wyman 1985), deflection (e.g., Miranda and James 1992), and periodic steepening above the mountain (Smith 1977). Blocking and deflection alter the total drag and cause some of it to be deposited at low levels close to the source. This part is referred to as nonpropagating.

The remaining term on the right-hand side of (10) could be included analytically by replacing (9) with

$$\langle \boldsymbol{\tau} \rangle = \frac{\bar{\rho} \bar{N}}{\rho_r N_r} (\langle \mathbf{T} \rangle \bar{\mathbf{V}} + \langle \mathbf{S} \rangle \bar{\mathbf{V}}_z), \quad (11)$$

where $\mathbf{S} = h \nabla \tilde{\chi} (\nabla h)^T$. However, this correction is less significant than the other two nonlinear effects when the local Richardson number, $\bar{N}^2 / (\bar{\mathbf{V}}_z)^2$, is large. The Richardson number is assumed to be large in making the WKB approximation leading to (5). Moreover, the uncertainty about the proper value of $\bar{\mathbf{V}}$ (and \bar{N}) to use when a planetary mixed layer is present could easily exceed the size of a correction for $\bar{\mathbf{V}}_z$.

The plan is to evaluate the nonpropagating drag associated with blocking mountains by resorting to dimensional analysis and assuming a fast orographic adjustment process (Pierrehumbert and Wyman 1985; Pierrehumbert 1987; Olafsson and Bougeault 1996). What follows is a fairly standard treatment along these lines (e.g., Lott and Miller 1997), except that it allows for a range of mountain heights within the grid cell. As mentioned briefly at the beginning, the motivation for adding complexity here is 1) to produce a better match between the linear drag and the dimensional estimate in the limit of small terrain and 2) to set up a more rational, less tunable, transition to partially blocked flow. Thus, the analytical result will be used to constrain the drag coefficient for propagating components,

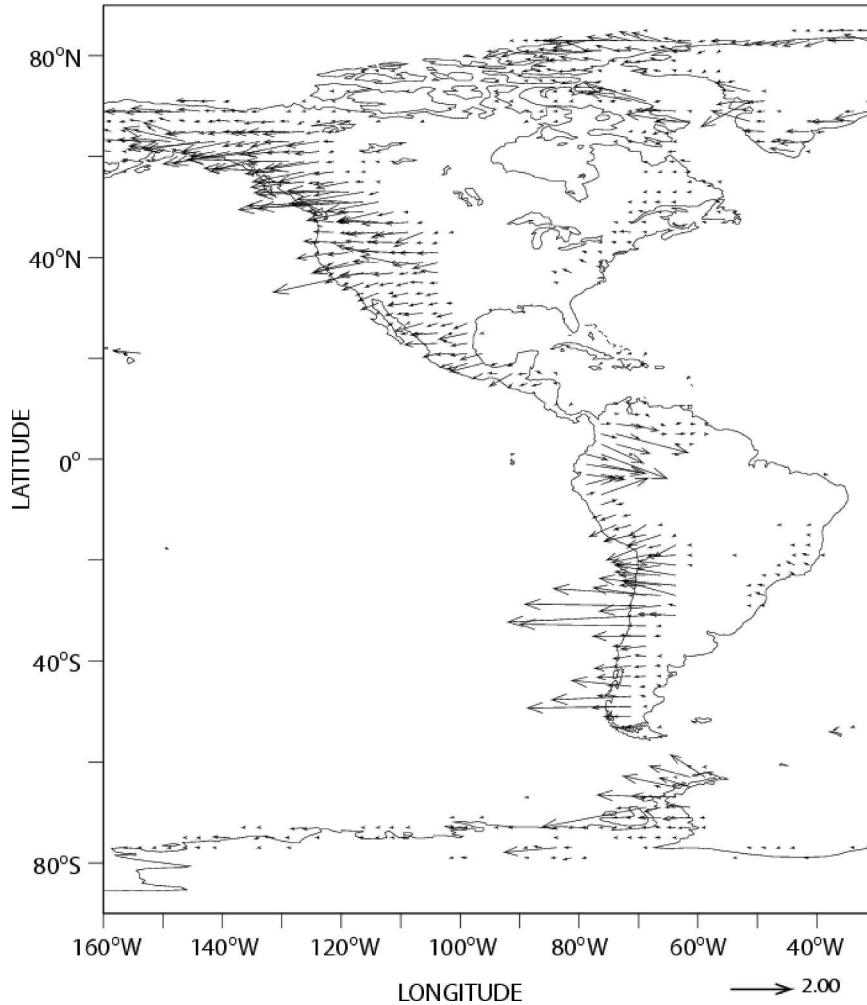


FIG. 1. The drag associated with stationary linear mountain waves over North and South America and western Antarctica. The assumed surface wind is purely zonal at -7 m s^{-1} in the Tropics and 13 m s^{-1} elsewhere. The assumed surface static stability and density are 0.01 s^{-1} and 1.0 kg m^{-3} , respectively. The arrow below the plot shows the scale for 2 Pa.

and this scaling, together with some assumptions about the mountain ensemble, will determine the transition to partially blocked flow. Since the excess mountain height responsible for blocking cannot be straightforwardly attributed to spectral components, the key assumptions here will be 1) that the topography is characterized by well-defined features, each with a well-defined areal extent, that can be binned into height ranges, and 2) that the flow disturbances induced by individual features do not interact strongly.

1) DRAG MODEL FOR INDIVIDUAL FEATURES

If the mountain height exceeds a certain threshold, h_c , that depends on both \bar{V} and \bar{N} , the flow is blocked or deflected below a level $z = h - h_c$. Here, h is being used

to represent the height of individual mountains, rather than a continuous distribution in space. For terrain features with heights less than h_c , the drag is entirely linear and propagating. For those greater than h_c , it includes a propagating and a nonpropagating contribution, as shown schematically in Fig. 3. The part that launches internal waves has a height of h_c , measuring down from the summit. To relate the width L of this part of the mountain to elevation above the base, a power law with parameter β is introduced:

$$L(z) = L_b(1 - z/h)^\beta. \tag{12}$$

Thus, $\beta = 1$ corresponds to triangular mountains, $\beta < 1$ to blunt mountains and $\beta > 1$ to pointed ones. This shape is a generalization of the one assumed by Lott and Miller (1997).

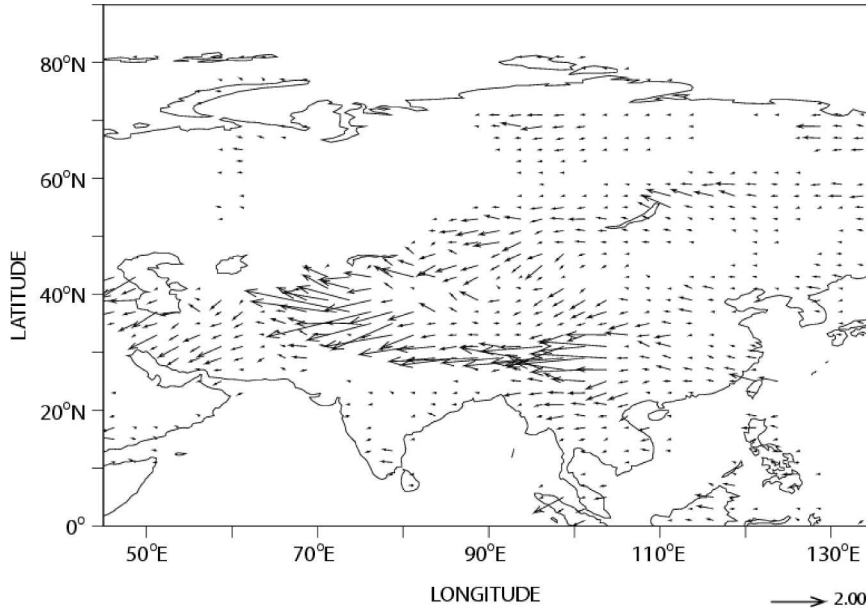


FIG. 2. The drag associated with stationary linear mountain waves over Asia. The assumed surface wind is purely zonal at 10 m s^{-1} everywhere. The assumed surface static stability and density are as in Fig. 1. The scale for 2 Pa is shown by the arrow below the plot.

As the flow becomes blocked by topography, the drag law in the blocked layer changes from $D_l \sim \rho N V h^2 / L$ to $D_{nl} \sim \rho V^2 (h - h_c) / L$, where V and L are the ambient wind component and length of the mountain, respectively, in the same direction. Orographic adjustment essentially means that the nondimensional depth $\tilde{h} = h(\bar{N}/\bar{V})$ of the unblocked, laminar flow below the summit is set by a universal threshold, $\tilde{h}_c = h_c(\bar{N}/\bar{V})$, related to the critical Froude number. The assumption that the blocked flow adjusts to the depth $z = h - h_c$ independently for each feature may be the weakest part of this closure.

To incorporate the tapering of the mountain, we refine the formula for the nonlinear drag per unit area as $D_{nl} \approx \rho V^2 \int L(z) dz / L_b^2$, with the integral ranging from zero to $h - h_c$. Then the total drag per unit area exerted by a mountain is sum of the two components,

$$D_p = a_0 \min[1, (\tilde{h}_c/\tilde{h})^{2-\beta}] \tilde{h}^2 (\bar{\rho} \bar{V}^3 / \bar{N} L_b),$$

$$D_{np} = a_1 [1 - \min[1, (\tilde{h}_c/\tilde{h})^{1+\beta}]] \frac{\tilde{h}}{1 + \beta} (\bar{\rho} \bar{V}^3 / \bar{N} L_b), \quad (13)$$

where D_p and D_{np} refer to the propagating and non-propagating parts of the base flux, respectively, and a_0 and a_1 are constant drag coefficients. This purely dimensional formulation is similar to that of Lott and Miller (1997) except that it limits the propagating drag to the saturation value when $\tilde{h} > \tilde{h}_c$ and does not assume $\beta = 1/2$. The parameter β appears in D_p because the propagating drag is inversely proportional to L . It appears in D_{np} because the vertical cross section, shown hatched in Fig. 3, is reduced by the tapering of the mountain when $\beta \neq 0$.

2) DRAG MODEL FOR THE GRID-CELL ENSEMBLE

Linear drag closures typically take L_b in (13) to be a universal constant and estimate \tilde{h}^2 as the mean-squared height of the filtered topography within the grid cell.

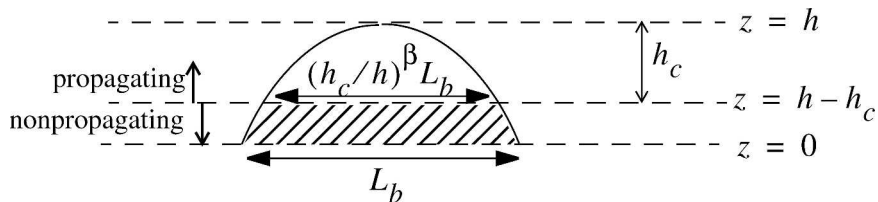


FIG. 3. Details of the scheme for separating the propagating part of the base flux from the nonpropagating (blocked or deflected) part. The hatched area is the cross section presented to the blocked or deflected part of the flow.

However, we have a better chance of matching the analytical drag if h and L_b are allowed to covary when averaging (13) over the grid cell. In the general case, with both $D_{np} \neq 0$ and $D_p \neq 0$, it is impractical to average explicitly over the subgrid height distribution because while \tilde{h}_c is assumed constant, \tilde{h} is time dependent.

We consider a particularly simple relationship between h and L_b that keeps the overall computation tractable. The analysis in the appendix suggests that we may assume a power law,

$$L/L_0 = (h/h_0)^\gamma, \quad (14)$$

where L_0 , h_0 , and γ are universal constants and L refers to L_b . Based on the analysis in the appendix, our best global estimate is $\gamma = 0.4$. Although the relation (14) seems to suggest a $-2/\gamma$ power spectrum for topographic height, it is actually a probability distribution across height bins rather than spectral components. The functional form of (14) satisfies the reasonable requirement of monotonicity and the practical requirement of closed-form integrability.

If we can neglect overlaps between mountains and ignore any correlation between anisotropy and mountain height, the areal coverage $dA \sim LdL$ of features in the range from \tilde{h} to $\tilde{h} + d\tilde{h}$ will be proportional to $n(\tilde{h})\tilde{h}^{2\gamma-1}d\tilde{h}$, where $n(\tilde{h})$ is the number of features in the range. For this number density we assume another power law, namely, $n(h) = n_1(h/h_1)^{-\varepsilon}$. We introduce $n(\tilde{h})$ mainly to acknowledge that it need not be unity: the value of ε used in the examples to follow is only a guess. The reasons for the specific functional form of $n(\tilde{h})$ are the same as for the relation (14), namely, monotonicity and integrability. Because of area averaging, the constants n_1 and h_1 will not appear in any results.

Since \bar{V} and \bar{N} are assumed constant over the grid cell, we can use the stated assumptions about the mountain height distribution to integrate (13) with respect to area and obtain

$$\begin{aligned} \langle D_p \rangle &= a_0 \frac{H^<(2 + \gamma - \varepsilon) + H^>(\gamma - \varepsilon - \beta)\tilde{h}_c^{2+\beta}}{H(2\gamma - \varepsilon)} \\ &\quad \times \tilde{h}_0^\gamma (\bar{\rho}\bar{V}^3/\bar{N}L_0) \\ \langle D_{np} \rangle &= a_1 \frac{H^>(1 + \gamma - \varepsilon) - H^>(\gamma - \varepsilon - \beta)\tilde{h}_c^{1+\beta}}{(1 + \beta)H(2\gamma - \varepsilon)} \\ &\quad \times \tilde{h}_0^\gamma (\bar{\rho}\bar{V}^3/\bar{N}L_0) \end{aligned} \quad (15)$$

for the average drag. Here $H(a) \equiv [(\tilde{h}_{\max})^a - (\tilde{h}_{\min})^a]/a$, and the superscript on H means that h is replaced with either $\tilde{h}^< \equiv \min(h, \tilde{h}_c)$ or $\tilde{h}^> \equiv \max(h, \tilde{h}_c)$. The limit for

small a is $H(0) = \log(\tilde{h}_{\max}/\tilde{h}_{\min})$. Note that the limits of the area integration have been transformed to height limits, h_{\min} and h_{\max} . The contribution from the partially blocked terrain in the numerator for D_p includes the effect of reducing the forcing area element dA by the factor $(\tilde{h}/\tilde{h}_c)^{-2\beta}$, as implied in Fig. 3. This sort of clipping from the sides is essentially the reverse of that described by Lindzen (1988) for the wave train itself.

The small-amplitude ($\tilde{h} \rightarrow 0$) limit of (15) is $\langle D \rangle \rightarrow D^*$, where

$$D^* \equiv a_0 \bar{\rho} \bar{N} \bar{V} \eta^2 / L_0 \quad (16)$$

and

$$\eta \equiv \frac{\bar{V}}{\bar{N}} \tilde{h}_0^{\gamma/2} \left[\frac{H(2 + \gamma - \varepsilon)}{H(2\gamma - \varepsilon)} \right]^{1/2}. \quad (17)$$

As noted above, traditional schemes for linear base flux use (16) with η identified as the root-mean-squared height of the filtered topography. However, with η given by (17), D^* is proportional to $\langle h^{2-\gamma} \rangle$, instead of $\langle h^2 \rangle$, reflecting the covariance of L and h . The lower moment when $\gamma > 0$ does yield a better universal match to the linear solution, as we show below. The ability to make the linear drag coefficient a weak function of latitude and longitude supports some of the foregoing assumptions and provides some confidence about the validity of the next step.

3) SCALING OF THE ANALYTICAL FLUX

From this point, the procedure to separate the drag into linear and nonlinear parts is straightforward. We let a_0 be determined by $D^* = |\langle \tau \rangle|$ with D^* defined by (16) and $\langle \tau \rangle$ by (9). Then we use this result in (13), allowing (9) to determine the direction of the drag. The resulting base flux, as modified by the bulk dimensional analysis, is

$$\langle \tau \rangle = \left(\frac{\langle D_p \rangle}{D^*} + \frac{\langle D_{np} \rangle}{D^*} \right) \tau^*, \quad (18)$$

where τ now refers to the corrected drag, and τ^* to the original linear result (9). Only the nonlinear drag coefficient a_1 (in the expression for D_{np}) is undetermined. The nonpropagating part of (18) is available for forcing the resolved momentum below a reference level, while the propagating part is available for distribution over the column according to a level-by-level determination of wave saturation. Note that the propagating fraction cannot exceed unity but the sum of the two parts does not have this constraint.

Although the linear drag coefficient a_0 is no longer explicit, the strategy for choosing V in the dimensional analysis should still be to minimize its variability in time and space. The direction of τ^* varies between that of

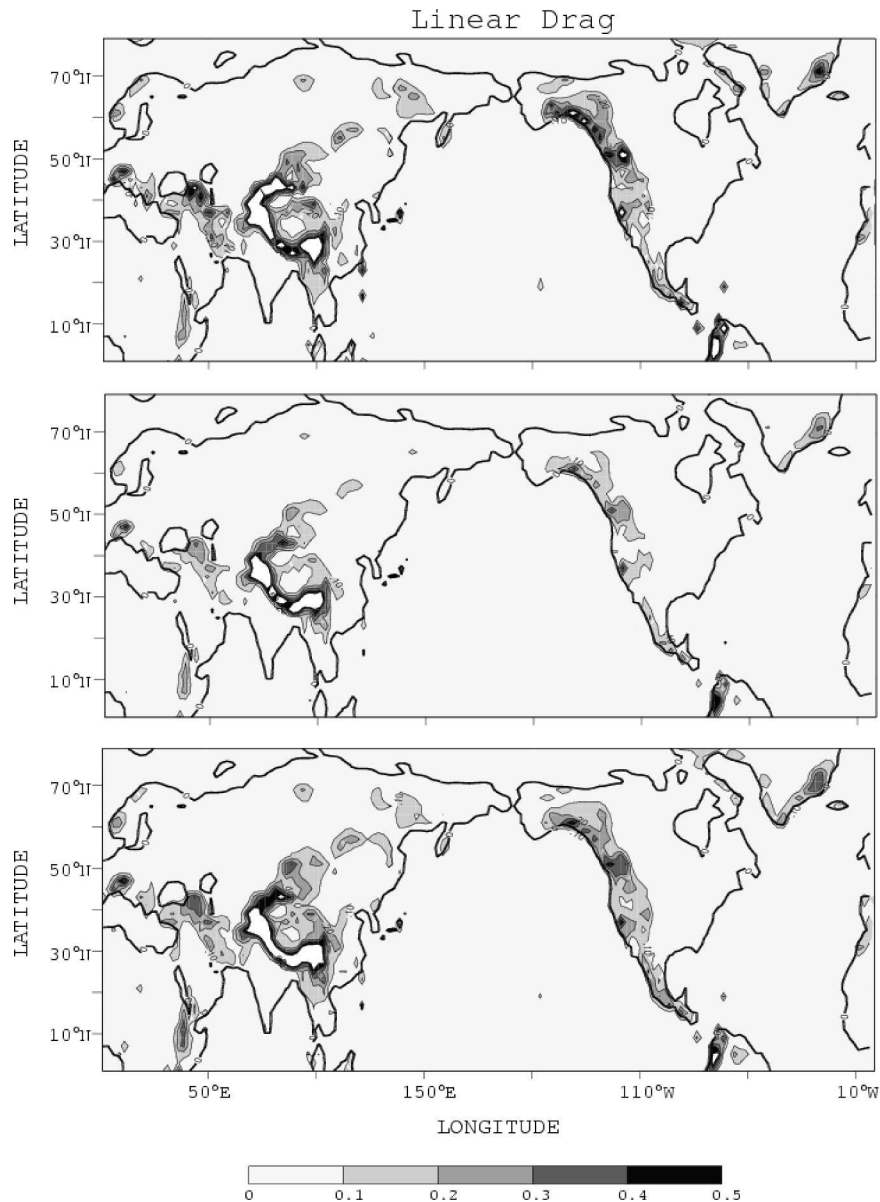


FIG. 4. The distribution over the Northern Hemisphere of the linear drag computed in three ways: (top) the analytical drag reduced to a scalar, (middle) the dimensional drag based on topographic variance, and (bottom) the dimensional drag based on (17) with $\gamma = 0.5$. Values are normalized by the respective global maxima, which occur in the Himalayas. The output grid has a resolution of 2.0° in latitude by 2.5° in longitude. The input grid is $1/30^\circ$ in both directions.

$-\bar{\mathbf{V}}$ in the case of isotropic terrain to that of the first eigenvector of \mathbf{T} in the case of strongly anisotropic terrain. In the latter case, the drag is insensitive to the component of $\bar{\mathbf{V}}$ in the direction of the second eigenvector, which is approximately orthogonal to the drag in that limit. Therefore, the traditional choice of taking V to be the component in the direction opposite the drag roughly optimizes the match between the dimensional and analytical drags with minimal variation in a_0 .

It also provides the physically relevant nondimensional mountain height, $\tilde{h} = Nh/V$, since Nh is the scale for the velocity perturbation in the drag direction for an individual mountain.

c. Illustrative examples

Figure 4 compares the distribution of linear base flux computed in three different ways. The top panel shows the analytical drag (9) evaluated in the scalar form

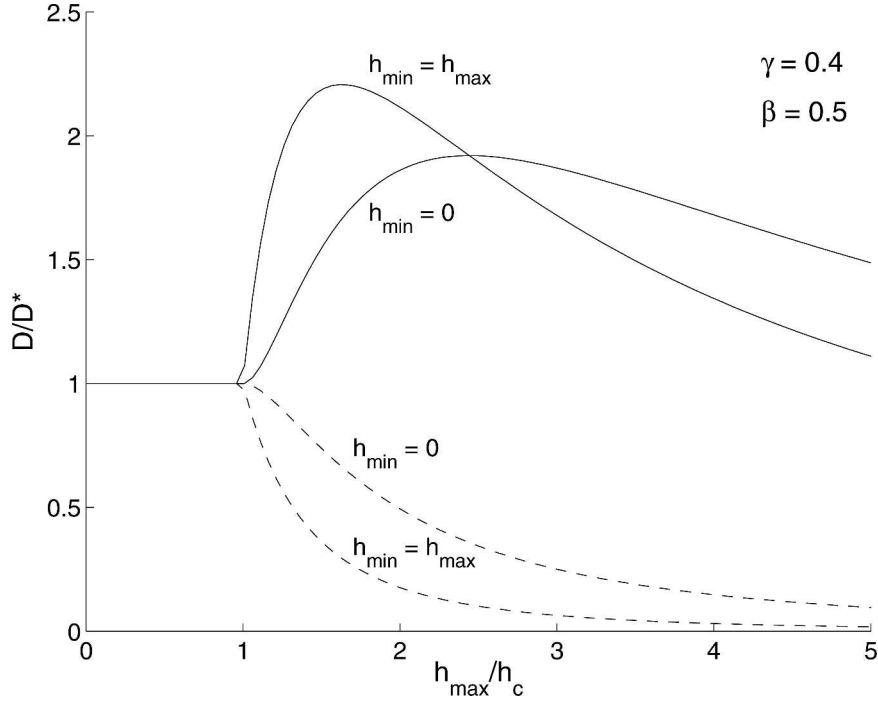


FIG. 5. Normalized estimates, based on dimensional analysis, of the propagating drag, $\langle D_p \rangle / D^*$ (dashed), and total drag, $\langle D_p + D_{np} \rangle / D^*$ (solid), as a function of normalized maximum mountain height, $\tilde{h}_{\max} / \tilde{h}_c$, for the two extreme cases $\tilde{h}_{\min} = 0$ and $\tilde{h}_{\min} = \tilde{h}_{\max}$ with $\gamma = 0.4$, $\beta = 0.5$, and $\varepsilon = 0$. The drag is normalized by the linear dimensional estimate D^* defined by (16) and (17). The nonpropagating part assumes $a_1/a_0 = 9.0\tilde{h}_c$.

$$D = \frac{\bar{\rho}}{\rho_r} \bar{V} \max(|T_1|, |T_2|), \quad (19)$$

where T_1 and T_2 are the eigenvalues of \mathbf{T} . The middle panel shows the traditional dimensional estimate using $\eta^2 = \langle h^2 \rangle$, the variance of the filtered topography, and the bottom panel is the new dimensional estimate, using (17) for η^2 . Each case uses a uniform \bar{V} and $\bar{\rho}$ and normalize the result by the maximum drag, which occurs in the Himalayas. Both dimensional estimates fall short of the analytical drag almost everywhere outside the Himalayan range, but the traditional estimate is quite a bit worse. The differences are most noticeable in Siberia and the central Rockies. Similar differences appear in the Andes and western Antarctica (not shown). As previously suggested, this is mainly because the dependence on h in (17) falls somewhere between the standard deviation and the mean topographic relief. The new result is based on $\gamma = 0.5$ (ε is irrelevant here for the reason mentioned just below). This choice for γ produces a slightly better match than the value suggested in the appendix.

For h_{\min} and h_{\max} , the actual minimum and maximum from the set of local extrema of high-pass topography within each cell were not used. There is a great deal of scatter in the height distribution, as shown in the appendix. To produce a less erratic estimate of the height

limits, the small-amplitude limit of D_p in (13) was averaged over the actual topographic data and equated to the small-amplitude limit of $\langle D_p \rangle$ in (15). This yielded the desired h_{\max} after assuming $h_{\min} = \mu h_{\max}$ for some fixed μ . This way of handling h_{\min} makes the linear drag estimate independent of ε . Since $h_{\min} \ll h_{\max}$ almost everywhere, the result is insensitive to μ for realistic choices. To integrate (13) over grid cells with band-passed data, the integrand was taken as proportional to $h^{2-\gamma}$ and summed directly over area instead of bins. Integrating with respect to area fails to hold h and L fixed across individual mountains, but the consequence, according to present assumptions, is a constant multiplicative factor that depends on the mountain shape and does not change the normalized drag. The condition $h > 0$ was enforced by subtracting the minimum value within a bandpass radius, with h nudged to zero in the far field to avoid discontinuities. The same thing was done to obtain the rms result. Although this is not exactly the traditional rms result, it is a better match with the analytical drag and therefore shows the separate impact of γ . For the result in the bottom panel of Fig. 4, $\mu = 0$.

The transition from linear flux to saturation flux for the two extreme cases of $\tilde{h}_{\min} / \tilde{h}_{\max}$ is shown in Fig. 5, in which $\langle D_p \rangle / D^*$ is graphed as a function of $\tilde{h}_{\max} / \tilde{h}_c$ with $\gamma = 0.4$, $\beta = 0.5$, and $\varepsilon = 0$. Also shown is the total

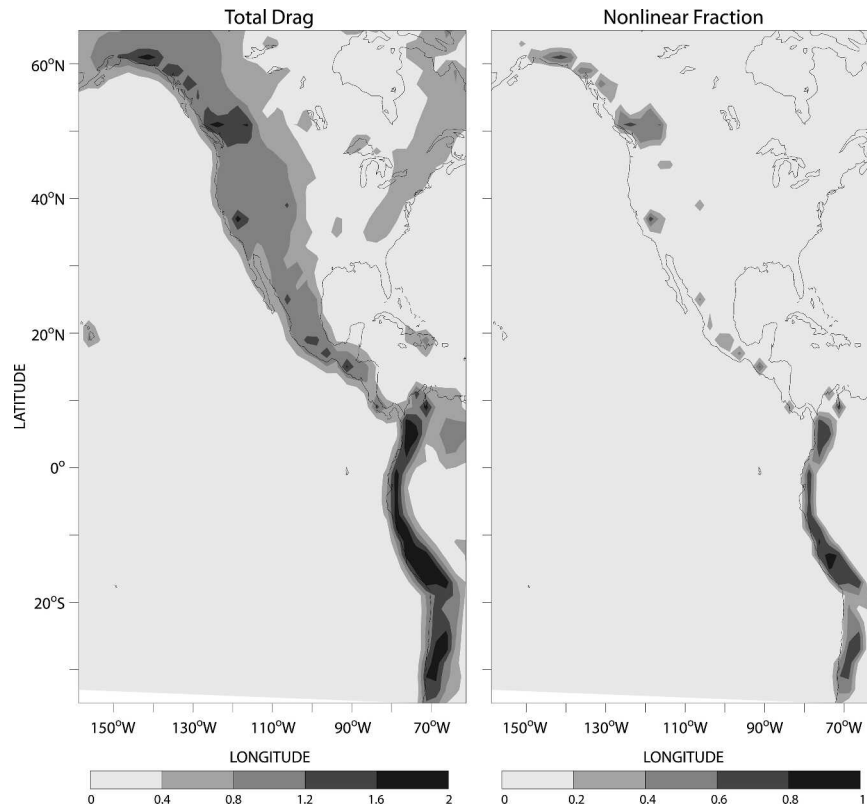


FIG. 6. The distribution over North and South America of the normalized (left) total base flux and (right) nonpropagating fraction, according to the bulk dimensional analysis, with $\gamma = 0.4$, $\beta = 0.5$, and $\varepsilon = 0$. The total flux is normalized by $D^* + 0.05$, where D^* is the small-amplitude limit and the small increment (in units of Pa) serves to mask out regions of weak forcing. The assumed large-scale surface wind is purely zonal at 10 m s^{-1} everywhere and the assumed static stability and density are as in Fig. 1. The input and output grids are the same as in Fig. 4. The critical mountain height is set to $\tilde{h}_c = 0.7$ to make the drag fully nonpropagating (blocked) only in the highest part of the Andes.

normalized drag $(\langle D_p \rangle + \langle D_{np} \rangle)/D^*$ based on the additional assumption that $a_1/a_0 = 9.0\tilde{h}_c$. This choice for a_1 produces a maximum total drag of approximately $2D^*$, which is a compromise between the maximum drags obtained in two- and three-dimensional nonlinear simulations, as summarized by Lott and Miller (1997) and Scinocca and McFarlane (2000). The sharpest transitions in both D_p and D_{np} occur for $\tilde{h}_{\max} \approx \tilde{h}_{\min}$. Results are less sensitive to γ , but large values of this parameter make the transitions sharper (not shown).

Shown in Fig. 6 is the bulk-dimensional drag for North America based on the same parameter choices as in Fig. 5. The assumed large-scale wind, needed for determining the range of \tilde{h} , is purely zonal at 10 m s^{-1} , and the static stability is $\bar{N} = 0.01 \text{ s}^{-1}$ everywhere. The critical mountain height, \tilde{h}_c , is taken to be 0.7. This is a tuning choice that will generally depend somewhat on the procedure for determining h_{\max} . With these choices, it is found that flow over the Rocky Mountains is

mostly linear, whereas the Himalayas (not shown) generate mostly nonlinear base flux.

3. Level-by-level determination of momentum forcing

To obtain the velocity tendency from $\partial \bar{\mathbf{V}}/\partial t = \dots - \bar{\rho}(z)^{-1} d\langle \tau \rangle/dz$, we need the vertical profile $\langle \tau(z) \rangle$. Let $\delta(z)$ denote the vertical particle displacement in a mountain wave and define $\tilde{h}(z) = \bar{N}\delta/\bar{V}$, where $\bar{N}(z)$ is the buoyancy frequency and $\bar{V}(z)$ is the resolved wind component in the direction opposite the net drag. Define $U(\tilde{h}, z) = \tilde{h}U_{\text{sat}}$, where $U_{\text{sat}}(z) = \sqrt{(\bar{\rho}/\rho_r)\bar{V}^3/\bar{N}L_0}$. Then $\rho_r U^2$ is proportional to the areally averaged pseudomomentum flux. The propagating part of the cell-averaged base flux (13) can now be expressed as

$$\begin{aligned} \langle D_p(0) \rangle = a_0 \frac{(2\gamma - \varepsilon)U_0^{\gamma-\varepsilon}}{U_{\max}^{2\gamma-\varepsilon} - U_{\min}^{2\gamma-\varepsilon}} \rho_r \\ \times (F_b + F_{ub}), \end{aligned} \quad (20)$$

where the contributions from the “broken” and “unbroken” parts of the field are, respectively,

$$F_b = \frac{U_{\max}^{\gamma'-\beta} - [U_c]^{\gamma'-\beta}}{\gamma' - \beta} U_c^{2+\beta}$$

$$F_{ub} = \frac{[U_c]^{2+\gamma'} - U_{\min}^{2+\gamma'}}{2 + \gamma'} \quad (21)$$

with $[U_c] \equiv \min[U_{\max}, \max(U_{\min}, U_c)]$ and $\gamma' = \gamma - \varepsilon$. This applies at $z = 0$. How does this flux change as a function of z as successive parts of the field attain $\tilde{h} = \tilde{h}_c$ and break?

The change to U in (20) is a z -dependent linear transformation of the original integration variable δ . According to the theorem of Eliassen and Palm (1960), the value of U associated with a particular feature is independent of z until that part of the field breaks. The unbroken components are the only parts of the flux that depend on the amplitude of the source feature, or U . This allows us to fix the integration limits, U_{\min} and U_{\max} , and move all z dependence in D_p to the saturation threshold U_c . The threshold is already z dependent because the saturation value of $\tilde{\delta}$ depends on the minimum value of $h_c = (\bar{V}/\bar{N})\tilde{h}_c$ (dimensional) in the underlying column. It is assumed that the horizontal scales of the individual features do not change as a result of wave breaking, so that U_0 , associated with the constants in (14), is not a function of z . Therefore, the z dependence in (20) is confined to F_b and F_{ub} .

Let $u_c(z) = \min_{z' \leq z} \{U_c(z')\}$. Then if the flux from each mountain is limited to the minimum of the saturation value, $D_c(z') \equiv \rho_r U_{\text{sat}}^2 \tilde{h}_c^2$, in the underlying column $z' < z$, the two parts of the flux $\langle D_p(z) \rangle$ are

$$F_b = \left[\frac{U_{\max}^{\gamma'-\beta} - [u_c(0)]^{\gamma'-\beta}}{\gamma' - \beta} u_c(0)^\beta + \frac{[u_c(0)]^{\gamma'} - [u_c]^{\gamma'}}{\gamma'} \right] u_c^2$$

$$F_{ub} = \frac{[u_c]^{2+\gamma'} - U_{\min}^{2+\gamma'}}{2 + \gamma'}, \quad (22)$$

where $[u_c] \equiv \min[U_{\max}, \max(U_{\min}, u_c)]$. The first contribution to F_b is due to components that were saturated at launch (hence the dependence on β), while the second is due to bins whose components have saturated above the ground. For the latter, we have assumed no horizontal clipping. We have also assumed that the disturbance cannot gain energy from the environment or reradiate from breaking regions (e.g., Bacheister and Schoeberl 1989). This means that, in layers where U_c increases with z , the residual flux from the broken components will hold constant at $\rho_r u_c^2 < D_c$, where $D_c \equiv \rho_r U_c^2$ is the local saturation value.

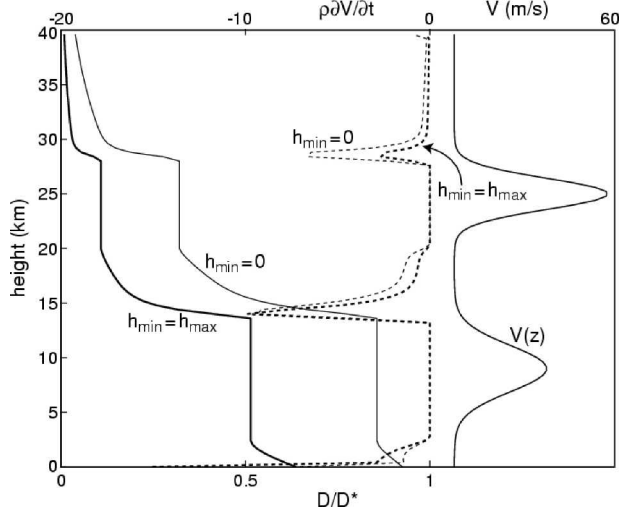


FIG. 7. The normalized pseudomomentum flux $\langle D_p \rangle / D^*$ (solid) and normalized momentum forcing (dashed) as a function of height for the two extreme cases $\tilde{h}_{\min} = 0$ and $\tilde{h}_{\min} = \tilde{h}_{\max}$ with $\gamma = 0.4$, $\beta = 0.5$, $\varepsilon = 0$, and $\tilde{h}_{\max} = 1.2\tilde{h}_c$. The assumed wind profile (shown at right) has jets of 38 and 58 m s^{-1} centered at heights of 9 and 25 km, respectively. The static stability increases from 0.011 to 0.022 s^{-1} across $z = 11$ km, and the assumed density scale height is 8 km. The momentum forcing is normalized by D^*/h .

Figure 7 is a graph of $\langle D_p(z) \rangle / D^*$, showing the transition to saturation as a function of height above the mountains for two different ranges of h and an assumed environmental column described in the caption. The dotted curves show the momentum forcing, which is proportional to the derivative of $\langle D_p(z) \rangle$. Pseudomomentum is deposited in the layers where D_p is decreasing with height, which, in this example, occur near the ground and just above the two assumed jets. The forced layers are broadened and full saturation is delayed when the terrain features within grid cells vary most widely in height ($\tilde{h}_{\min}/\tilde{h}_{\max} = 0$).

4. Time-varying resolved flow

The steady problem is the limit in which advective time scales are much shorter than time scales of the background flow. If one simplifies to a single background frequency, ω_0 , the limit is expressed as $\bar{V}_k |\mathbf{k}| \gg |\omega_0|$. The opposite limit, $\bar{V}_k |\mathbf{k}| \ll |\omega_0|$, is nearly as straightforward as the steady limit [Bell (1975) gives the linear topographic wave solution in the general case]. I show here that the resulting drag formula is almost the same as in the steady limit. We obtain the total drag by integrating

$$\boldsymbol{\tau}(x, y) = -\rho' \nabla(h + \delta') \quad (23)$$

along a streamline and substituting the limiting solution for pressure perturbation p' , and wave displacement,

$$\delta' \sim (\bar{V}_k |\mathbf{k}| / |\omega_0|) h.$$

In the unsteady problem, the eddy momentum flux (7) and the form drag (23) are not interchangeable.¹

If $|\omega_0| \gg \bar{V}_k |\mathbf{k}|$, we can proceed from (2) using $m \approx -\bar{N} |\mathbf{k}| \operatorname{sgn}(\omega_0) / \sqrt{\omega_0^2 - f^2}$ for the vertical wavenumber. Here f is the (slowly varying) Coriolis parameter and hydrostatic waves are assumed by taking $|\omega_0| \ll \bar{N}$. Then (3) is replaced by

$$\partial(\bar{\rho} \hat{w}) / \partial z = \bar{\rho} \left(-\frac{i \bar{N} |\mathbf{k}|}{\omega_0 \alpha} - \frac{1}{2H} \right) i |\mathbf{k}| \bar{V}_k \hat{h}, \quad (24)$$

where $\alpha \equiv \sqrt{1 - f^2 / \omega_0^2}$ and \bar{V}_k is the amplitude of the velocity oscillation projected onto the wavenumber vector. We still have that $\partial(\bar{\rho} w) / \partial z = -\nabla \cdot \bar{\rho} \mathbf{V}'$, and since the momentum equation implies

$$\left(\frac{\partial^2}{\partial t^2} + f^2 \right) (-\nabla \cdot \bar{\rho} \mathbf{V}') = \frac{\partial}{\partial t} \nabla^2 p', \quad (25)$$

we may operate on (24) with the transform equivalent of $\nabla^{-2} f dt(\partial^2 / \partial t^2 + f^2)$ to reach

$$\hat{p} = \bar{\rho} \left(\frac{\bar{N} \alpha}{|\mathbf{k}|} - \frac{\alpha^2}{2H |\mathbf{k}|^2} i \omega_0 \right) i |\mathbf{k}| \bar{V}_k \hat{h}. \quad (26)$$

If $|\omega_0| > |f|$, the first term in (26) produces

$$p_0 = -\alpha \nabla \chi_0 \cdot \bar{\mathbf{V}}, \quad (27)$$

where χ_0 is defined by (5) or (6). In this case, $\nabla \chi_0$ is not the momentum perturbation. The correction for the mean density gradient, say \hat{p}_1 , can be evaluated in terms of the field $A(x, y)$ defined earlier. We find that

$$p_1 = \bar{\rho} \frac{\alpha^2}{2H} \frac{\partial \bar{\mathbf{V}}}{\partial t} \cdot \nabla A. \quad (28)$$

However, the pressure perturbation is dominated by p_0

¹The high-frequency limit is determined by the terms $n = \pm 1$ in the solution by Bannon and Zehnder (1985). Note, however, that their passing remark about the surface pressure in this limit is incorrect: the pressure perturbation does not vanish but is given by (26) below.

where $\lambda = H$. Since $|\omega_0| \ll \bar{N}$, this requires that $|k|H \geq O(1)$.

We now put $\delta' = 0$ in (23) and substitute from (27) and (28) for the pressure. This yields

$$\tau = \alpha [\nabla \chi_0 (\nabla h)^T] \bar{\mathbf{V}} + O(\lambda/H), \quad (29)$$

which is the same as in the stationary case (8) except for the factor α and the different correction for mean density gradient. This result is directly relevant to internal waves generated by semidiurnal or higher-frequency tidal flows in the ocean (Arbic et al. 2004). It also applies to more general forcing with $|\omega| \gg |f|$, because the frequency dependence is weak in that limit.

Nonlinearity in the oscillatory limit is measured by the ratio $r = |\nabla \cdot \bar{\mathbf{V}}'| / |\omega_0|$, where $\bar{\mathbf{V}}'(x, y)$ refers to the amplitude of the oscillating velocity perturbation. This can be seen by writing the horizontal advection as $(\nabla \cdot \mathbf{V}') \mathbf{V}' - \nabla \cdot \mathbf{V}' \mathbf{V}'$ and exploiting Gauss's Law and the far-field weakness of the horizontal flux. Then, from (24) and mass continuity, the nonlinearity is essentially

$$r \approx \frac{|\nabla^2 h|}{\alpha \omega_0^2} \bar{N} \bar{V}. \quad (30)$$

This gives, among other things, the ratio of the nonlinear to the linear dimensional drag estimates. Unlike the analogous parameter, $\tilde{h} \equiv \bar{N} h / \bar{V}$, for the steady problem, r depends on the horizontal scale L of the forcing, since $|\nabla^2 h| \sim h / L^2$. This will affect the nonlinear part of the base flux in the manner described next.

For the maximum or time-averaged linear drag, we have $D_l \sim \bar{\rho} \alpha \bar{N} \bar{V} h^2 / L$ (reverting to the discrete meaning of h). The saturation drag D_{sat} is estimated by substituting for h in this expression, using (30) and $r = 1$. Thus, $D_{\text{sat}} \sim \bar{\rho} \alpha^3 \omega_0^4 L^3 / \bar{N} \bar{V}$. In view of (29), we should normalize topographic heights according to

$$\tilde{h} = \alpha^{-1} \left(\frac{\bar{V}}{\omega_0 L_0} \right)^2 \frac{\bar{N} h}{\bar{V}}. \quad (31)$$

Then the average drag is calculated in the same way as (15), using the relations (12) and (14) for the horizontal scale. We find that

$$\begin{aligned} \langle D_p \rangle &= a_0 \tilde{h}_0^\gamma \frac{H^<(2 + \gamma - \varepsilon) + H^>(5\gamma - \varepsilon + 3\beta)(\tilde{h}_0^{-4\gamma} \tilde{h}_c^{2-3\beta})}{H(2\gamma - \varepsilon)} (\bar{\rho} \alpha^3 \omega_0^4 L_0^3 / \bar{N} \bar{V}), \\ \langle D_{np} \rangle &= a_1 \tilde{h}_0^{-3\gamma} \frac{H^>(1 + 5\gamma - \varepsilon) - H^<(5\gamma - \varepsilon - \beta) \tilde{h}_c^{1+\beta}}{(1 + \beta)H(2\gamma - \varepsilon)} (\bar{\rho} \alpha^3 \omega_0^4 L_0^3 / \bar{N} \bar{V}). \end{aligned} \quad (32)$$

Velocities are unbounded where $|\omega_0| = \pm |f|$ because of resonance, but the pressure perturbation and the drag both vanish as these latitudes are approached from the equator (the saturation drag does so quite gradu-

ally). It follows from (31) that the drag becomes more and more linear (and D_{np} eventually drops out) as $\bar{V} \rightarrow 0$. Differences in the exponents compared to (15) are due to the new dependence on horizontal scale. The

Eliassen–Palm constraint that underlies the traditional diagnosis of wave breaking still applies to the maximum (or time-averaged) stress during the oscillation. The alterations to the vertical flux profile, given in the steady case by (21) and (22), are straightforward.

For the earth's semidiurnal tides, $\omega_0 \approx 1.4 \times 10^{-4} \text{ s}^{-1}$. Then since the deep ocean tidal amplitude is $\bar{V} \approx 0.02 \text{ ms}^{-1}$ (e.g., Arbic et al. 2004). The oscillatory limit is valid only at horizontal half-wavelengths, $\lambda_h = \pi/|\mathbf{k}|$, much greater than about 400 m. Near this transitional scale, (31) implies that h must be of order \bar{V}/\bar{N} , or about 100 m, in order to produce a nonlinear response (the factor α is irrelevant because the saturation drag is negligible near the resonant latitudes). At 10 times the transitional scale, that is, at the scale of present-day global bathymetric datasets, h must be 2 orders of magnitude larger, or about 10 km, to produce a nonlinear response. Therefore, nonlinearity in the oscillatory limit is confined to an extremely narrow range of horizontal scales. Nonlinear drag on the semidiurnal tide is likely to be dominated by scales shorter than 400 m, where the disturbance should behave at any given tidal phase as though the background flow were steady. In this range of scales, the forcing has to be extrapolated from data. A semiempirical relation like (14) might serve that purpose well enough.

5. Summary

Linear analysis gives the vector drag due to stationary, hydrostatic, nonrotating internal waves forced by arbitrary topography. Therefore, statistical or dimensional characterizations of the subgrid terrain are not required for the linear base-flux computation at most of the relevant spatial scales. It turns out that the linear base-flux formula in the case of an unsteady resolved flow is virtually identical to that for a steady background flow if the dominant frequencies satisfy $\omega \gg \bar{V}_k/|\mathbf{k}|$, $\omega \ll \bar{N}$ and $\omega > f$.

The analytical drag can be made part of a practical closure for atmospheric general circulation models. The analysis in the unsteady case could be used for parameterizing topographic drag due to semidiurnal tidal oscillations in the ocean. The correction for nonlinearity and the related formula for saturation flux continue to require an ad hoc treatment. I have suggested a dimensional treatment of the nonlinearity that takes maximal advantage of the linear solutions. Dimensional analysis indicates that most of the nonlinearity in the semidiurnal ocean tide is captured by the steady-state limit.

The base-flux scheme of Stern and Pierrehumbert (1988), to take one example, is essentially

$$D = G \frac{\tilde{h}^2}{a^2 + \tilde{h}^2} \rho V^3 / NL, \quad (33)$$

in which G and a are fixed parameters. Analogous parameters are needed by more sophisticated schemes, including those of Baines and Palmer (1990), Lott and

Miller (1997), and Scinocca and McFarlane (2000). The present approach eliminates the first of the two parameters (the linear drag coefficient) by providing the amplitude of the linear drag. It also provides the direction of the drag. The other parameter, a , is both the critical mountain height and part of the nonlinear drag coefficient, while the actual function chosen for the transition to nonlinearity is arbitrary. In the present scheme, the critical mountain height, \tilde{h}_c , and the nonlinear drag coefficient, a_1 , remain free parameters. However, the functional form of the transition is less arbitrary because (15) incorporates information about the range of mountain heights within each grid cell, subject to an assumed power law relation (14) between mountain height and width.

The present approach to the problem of drag closure makes it possible to use statistics much more sparingly than in previous schemes. The use of statistics has been reduced to a one-parameter height–width relation used to separate the nonpropagating from the propagating drag, and this is tightly constrained by the analytical result. For base-flux estimates in strongly blocking regimes, it is not known whether the nonpropagating drag estimate improves on methods that rely more fundamentally on statistical representations of the unresolved topography. However, the propagating part of the base flux estimate is preferable because the linear analysis extracts the most relevant information from the terrain data. The improvement almost certainly extends to mountains that are marginally blocking.

Above the mountains, the sharpness of the transition to saturation determines the depth of the layers subjected to momentum forcing. The forcing is therefore broadened by the proposed ensemble integration. Broadening due to nonparallel vertical shear and subgrid variation of drag orientation (Shutts 1995) is missing from the scheme. For real topography, there is no universal relationship between the subgrid drag orientation and subgrid mountain height, which would be needed to make a simple correction to (21) for rotational shear. A credible solution may be to introduce a probability distribution for drag angles analogous to, but independent of, (14). The ensemble integration would then be two-dimensional.

Acknowledgments. I am grateful to Brian Arbic for checking the analysis. I also benefited from discussions with Isaac Held, Jonas Nycander, and John Scinocca about implementation and applicability. I thank Amy Braverman for some good advice on analyzing the scatterplots.

APPENDIX

Constraint on the $h(L)$ Relationship

Whether the relationship assumed in (14) is reasonable can be judged from scatterplots of log height versus log width of actual terrain features. A naive ap-

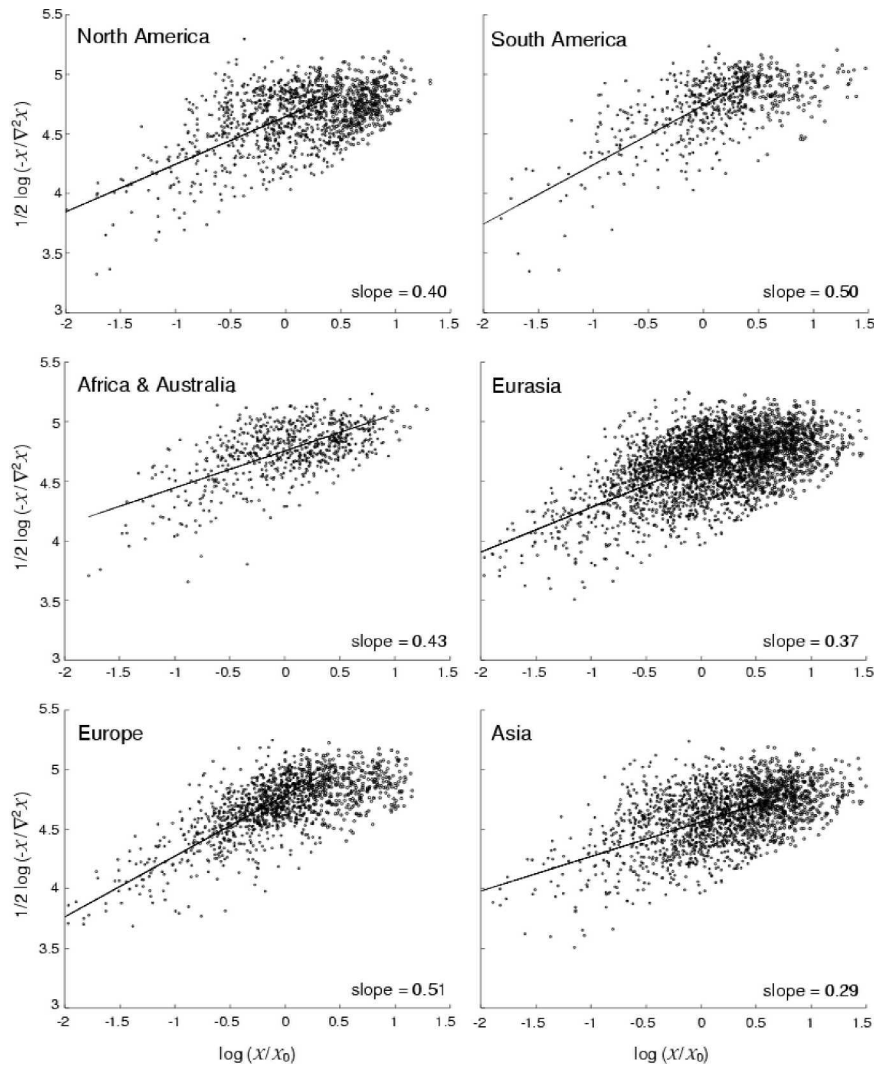


FIG. A1. Scatterplots of mountain width vs mountain height on log–log axes for six geographical regions. Width (ordinate) is estimated from the finite-difference Laplacian of the velocity potential, and height (abscissa) is identified with the velocity potential itself, referred to the local minimum value. Correlation coefficients range from 0.2 to 0.3. The line segments show the orientation of the principal components of the distributions excluding the largest features (see text), with the slope values indicated at the bottom right of each plot.

proach to generating these values from the bandpassed data is as follows. A terrain feature is considered to be any local maximum. Local minima are ignored because they would presumably share a width scale with a nearby maximum. This allows us to enforce $h > 0$, as was done in the nonlinear drag analysis, by referring heights to the minimum value observed within the local bandpass radius. The widths are then estimated from the finite-difference Laplacian of the terrain height normalized by the height itself.

The result of using the topographic data directly in these calculations is an essentially flat distribution of width that is dominated by the scale of the input grid. This is because the derivatives in the Laplacian opera-

tor strongly favor the smallest scales. To get a better picture of the mountain shape distribution, I instead perform the same analysis on the velocity potential (6), which is a horizontal integral of height.

The plots in Fig. A1 focus on six geographical regions. The abscissa is the logarithm of normalized velocity potential, and the ordinate is the logarithm of the aforementioned function of velocity potential that can be interpreted as the width scale, namely the square root of $A = -\chi/\nabla^2\chi$. The clustering of points near the mean is exaggerated by the filtering. Although the positive sign of the correlation is unambiguous, the scatter is considerable (with correlation coefficients of only 0.2 to 0.3) and difficult to distill.

With this in mind, I have drawn, for each of the six regions, the principal component axis for a subset of the distribution formed by ignoring the largest scales. The justification for leaving out the largest scales is that the width computation at that end is strongly affected by interference from smaller features. When features are not cleanly separated, the distribution becomes flat. The slopes of the principal component axes for the full distributions are generally 0.1 to 0.2, but when we exclude the mountains with dimension exceeding twice the mean (measured along the principal axis) one gets the steeper slopes recorded in the plots. These range from about 0.3 to 0.5. Based on this analysis, I would settle on $\gamma = 0.4 \pm 0.1$ for the parameter in (14), with the largest values for the Andes and the Alps, and the smallest values for the Himalayas.

REFERENCES

- Arbic, B. K., S. T. Garner, R. W. Hallberg, and H. L. Simmons, 2004: The accuracy of surface elevations in forward global barotropic and baroclinic tide models. *Deep-Sea Res.*, **51B**, 3069–3101.
- Bacmeister, J. T., 1993: Mountain-wave drag in the stratosphere and mesosphere inferred from observed winds and a simple mountain-wave parameterization scheme. *J. Atmos. Sci.*, **50**, 377–399.
- , and M. R. Schoeberl, 1989: Breakdown of vertically propagating two-dimensional gravity waves forced by orography. *J. Atmos. Sci.*, **46**, 2109–2134.
- Baines, P. G., and T. N. Palmer, 1985: Rationale for a new physically based parameterization of subgridscale orographic effects. Tech. Memo. 169, European Centre for Medium-Range Weather Forecasts, 11 pp.
- Bannon, P. R., and J. A. Zehnder, 1985: Surface pressure and mountain drag for transient airflow over a mountain ridge. *J. Atmos. Sci.*, **42**, 2454–2462.
- Bell, T. H., 1975: Lee waves in stratified flows with simple harmonic time dependence. *J. Fluid Mech.*, **67-4**, 705–722.
- Eliassen, A., and E. Palm, 1960: On the transfer of energy in stationary mountain waves. *Geophys. Publ.*, **22**, 1–23.
- Holton, J. R., 1973: *An Introduction to Dynamical Meteorology*. Academic Press, 361 pp.
- Kim, Y.-J., and A. Arakawa, 1995: Improvement of orographic gravity wave parameterization using a mesoscale gravity wave model. *J. Atmos. Sci.*, **52**, 1875–1902.
- Lindzen, R. S., 1981: Turbulence and stress due to gravity wave and tidal breakdown. *J. Geophys. Res.*, **86**, 9707–9714.
- , 1988: Supersaturation of vertically propagating internal gravity waves. *J. Atmos. Sci.*, **45**, 705–711.
- Lott, F., and M. J. Miller, 1997: A new subgrid-scale orographic drag parameterization: Its formulation and testing. *Quart. J. Roy. Meteor. Soc.*, **123**, 101–127.
- Miranda, M. A., and I. N. James, 1992: Non-linear three-dimensional effects on gravity-wave drag: Splitting flow and breaking waves. *Quart. J. Roy. Meteor. Soc.*, **118**, 1057–1081.
- Olafsson, H., and P. Bougeault, 1996: Nonlinear flow past an elliptic mountain ridge. *J. Atmos. Sci.*, **53**, 2465–2489.
- Palmer, T. N., G. J. Shutts, and R. Swinbank, 1986: Alleviation of a systematic westerly bias in general circulation and numerical weather prediction models through an orographic gravity wave drag parameterization. *Quart. J. Roy. Meteor. Soc.*, **112**, 1001–1039.
- Pierrehumbert, R. T., 1987: An essay on the parametrization of orographic gravity wave drag. *Proc. Seminar/Workshop on Observations, Theory and Modeling of Orographic Effects*, Vol. 1, Shinfield Park, Reading, United Kingdom, ECMWF, 251–282.
- , and B. Wyman, 1985: Upstream effects of mesoscale mountains. *J. Atmos. Sci.*, **42**, 977–1003.
- Scinocca, J. F., and N. A. McFarlane, 2000: The parameterization of drag induced by stratified flow over anisotropic orography. *Quart. J. Roy. Meteor. Soc.*, **126**, 2353–2393.
- Shutts, G., 1995: Gravity-wave drag parameterization over complex terrain: The effect of critical-level absorption in directional wind-shear. *Quart. J. Roy. Meteor. Soc.*, **121**, 1005–1021.
- Smith, R. B., 1977: The steepening of hydrostatic mountain waves. *J. Atmos. Sci.*, **34**, 1634–1654.
- Stern, W. F., and R. T. Pierrehumbert, 1988: The impact of an orographic gravity-wave drag parameterization on extended range prediction with a GCM. Preprints, *Eight Conf. on Numerical Weather Prediction*, Baltimore, MD, Amer. Meteor. Soc., 745–750.